Correspondence to:
S. J. T. Hangx,
S.J.T.Hangx@uu.nl

Micromechanics of High-Pressure Compaction in Granular Quartz Aggregates

Suzanne J. T. Hangx[1] and **Nicolas Brantut[2]**

[1]Department of Earth Sciences, Faculty of Geosciences, Utrecht University, Utrecht, Netherlands, [2]Department of Earth Sciences, University College London, London, UK

Abstract The mechanical behavior of porous sandstones is generally modeled using concepts from granular mechanics, often overlooking the effect of cementation. To probe the key differences between sand and sandstone mechanics, we performed triaxial deformation experiments on Ottawa quartz sand at 5- to 40 MPa effective confining pressure. At 5 MPa, the samples are able to dilate. At higher confinement, the aggregates show continuous compaction, displaying strain hardening. The stress-strain behavior is nonlinear, and the exact onset of inelastic compaction could not be determined accurately. Measured *P*-wave velocities show the development of anisotropy. With increasing axial strain, the along-axis velocities tend to increase, while velocities perpendicular to the compression axis tend to decrease (at low pressure) or remain constant (at high pressure). In samples deformed under elevated pressure conditions, acoustic emission event locations are diffuse. Microstructural investigations show an increase in grain chipping and crushing with increasing confining pressure, but no evidence of localized compaction could be observed. The nature of the pore fluid, either decane or water, does not significantly influence the mechanical behavior at strain rates of 10^{-6} to 10^{-4} s^{-1}. Grain angularity and grain-size distribution also did not significantly change the mechanical behavior. We infer that our observations indicate that the lack of cementation introduces additional degrees of freedom for grains to slide, rotate, and reorganize at the sample scale, precluding the existence and sustainability of stress concentrations beyond the grain scale. This results in progressive compaction and hardening, and lack of compaction localization.

1. Introduction

Highly porous unconsolidated sands and poorly consolidated sandstones (porosity $\geq$ 20%) constitute important reservoirs targeted for hydrocarbon extraction (e.g., Gulf of Mexico—Li et al., 2003; Ostermeier, 1995; Slochteren Sandstone, Groningen Gas Field, the Netherlands—Hettema et al., 2002). It is their high porosity that makes such reservoirs suitable for fluid production due to the often high permeability. However, changes in effective overburden stress due to fluid extraction can result in compaction at the reservoir level. Even relatively small amounts of compactive strain (few tenths of a percent) can lead to surface subsidence and induced seismicity (Doornhof et al., 2006; Pijnenburg et al., 2018, 2019; Spetzler & Dost, 2017), while larger strains (several percent) and strain localization can lead to geotechnical problems, such a wellbore casing collapse (Doornhof et al., 2006; Li et al., 2003), or reduce reservoir permeability impacting production (Olsson et al., 2002). Compaction is most likely caused by a direct poro-elastic response (Wang, 2000) and time- or rate-independent inelastic compaction, as well as time-dependent compaction creep, which may continue long after production has ceased (Doornhof et al., 2006).

Porous sandstones have been extensively studied, and a vast body of work is dedicated to deformation and strain localization in sandstone (see Wong & Baud, 2012, and references therein). At very low confining pressure, strain localization in porous sandstones has been shown to occur via dilatant shear localization moving to compactant shear localization at low-to-moderate confinement (Wong & Baud, 2012). At higher confining pressures, compaction may transition toward strain localization via discrete (Fortin et al., 2007; Heap et al., 2015; Klein et al., 2001; Louis et al., 2006; Tembe et al., 2008) or diffuse compaction bands (Baud et al., 2004; Olsson & Holcomb, 2000; Olsson et al., 2002) to distributed cataclastic flow under hydrostatic conditions (Baud et al., 2004). While discrete compaction bands (i.e., $\leq$3 grains wide; Baud et al., 2004) may be formed under both constant strain rate and constant stress conditions (Heap et al., 2015), they have been observed in very few sandstones deformed under laboratory conditions. It is believed that discrete com-

paction bands are promoted in high porosity (≥20%), well-sorted, and spatially homogeneous sandstones (Cheung et al., 2012), such as the Bentheim, Bleurswiller, and Diemelstadt sandstone (Fortin et al., 2007; Heap et al., 2015; Louis et al., 2006; Tembe et al., 2008). Furthermore, under wet conditions, sandstones generally tend be significantly weaker (Baud, Zhu, et al., 2000; Duda & Renner, 2012).

Studies on the uniaxial consolidation (porosity loss) behavior of sands are numerous, focusing on the effect of grain-size and angularity, mineralogy, and chemical environment (Brzesowsky, Hangx, et al., 2014; Brzesowsky, Spiers, et al., 2014; Chuhan et al., 2003, 2002; Fawad et al., 2011; Mesri & Vardhanabhuti, 2009). These studies show that higher initial porosity, increasing grain angularity, increasing grain-size and size uniformity, decreasing intrinsic grain strength, and the presence of aqueous fluids enhance consolidation (Brzesowsky, Hangx, et al., 2014; Brzesowsky, Spiers, et al., 2014; ; Chuhan et al., 2003, 2002; Hangx et al., 2010; Lee & Farhoomand, 1967; Vesíc & Clough, 1968; Zoback & Byerlee, 1976). Initial consolidation of sand is attributed to tighter packing promoting particle locking, while upon higher stresses interparticle slip and particle crushing and fracturing lead to further particle unlocking and concomitant compaction (Mesri & Vardhanabhuti, 2009; Muñoz-Ibáñez et al., 2019). Additionally, many studies exist in the soil mechanics community, regarding triaxial consolidation of sands and clays, though often at low confining pressures (e.g., see Alikarami et al., 2015; Pestana et al., 2002). Under low confining conditions (confining pressures of 0.1–7 MPa), recent experiments using X-ray computed tomography show the formation of dilation and compaction shear bands (Alikarami et al., 2015), accommodated by grain rolling and frictional sliding (Alikarami et al., 2015; Karner et al., 2005). Grain angularity impacts compaction and strain localization behavior by enhancing interlocking in more angular aggregates, which in turn inhibits dilation (Alikarami et al., 2015; Guo & Xubin, 2007). However, systematic experimental study of the micromechanics of strain localization in unconsolidated sands at higher confinement has received much less attention (Karner et al., 2005; Nguyen et al., 2014; Skurtveit et al., 2013).

Instead, extensive numerical modeling efforts have been made to predict the behavior of compacting sands and sandstones, either through constitutive modeling (Buscarnera & Laverack, 2014; Choo & Lee, 2018; Einav, 2007; Issen & Rudnicki, 2000; Pestana & Whittle, 1999; Tengattini et al., 2014) or employing particle models such as discrete elements (Marketos & Bolton, 2009; Potyondy & Cundall, 2004; Wang et al., 2008; Wu et al., 2018). Such numerical models are crucial in providing the means to extrapolate granular material behavior across spatial and temporal scales. However, they generally assume that rocks can be approximated as grains held together by cement bonds (e.g., see Einav, 2007; Potyondy & Cundall, 2004). This would imply that once sufficient cement bonds are broken, the material would essentially behave as a loose granular aggregate, as confirmed by low-confinement experiments on loose sand and artificially cemented sand (Bernabé et al., 1992). While compaction bands in sand have not been experimentally verified, discrete element modeling efforts have suggested that it is possible to generate compaction bands in sand packs, though less pronounced than in sandstones (Marketos & Bolton, 2009).

Given the first-order similarities in mechanical behavior between sands and sandstones, and the effectiveness of granular microphysical models to explain the deformation of sandstones, should imply that unconsolidated sand aggregates behave in the same way as sandstones. This would mean that in sand the onset of inelastic compaction is driven by the onset of grain crushing at the microscale. It also implies that shear bands will develop at low confinement (Wong & Baud, 2012), while compaction bands should be observed at high confining pressure (P_c) if the grain size is narrowly distributed (Cheung et al., 2012; Wong & Baud, 2012). It should be noted that though this implies the assumption of a double-yield cap model, it has been shown that upon deformation of porous aggregates, and the concomitant compaction and porosity reduction, the initial yield cap can expand (e.g., Bedford et al., 2018; Pijnenburg et al., 2019; Wong et al., 1992; Xiao & Evans, 2003). Essentially this means that any material has the potential to transition from one side of the yield cap to the other, while the yield cap expands, regardless of how the material is deforming. Experiments have already shown that at low confinement, dilatant shear bands do form in loose sand (Alikarami et al., 2015), similar to porous sandstones (Wong & Baud, 2012). However, while sand experiments performed at higher confining pressure show significant grain crushing, as also seen seen in sandstones (Karner et al., 2005; Zoback & Byerlee, 1976), the micromechanical characteristics of strain localization in this regime remain unclear.

We performed a series of triaxial deformation experiments on homogeneous, highly porous, unconsolidated quartz sand aggregates at effective confining pressures in the range 5–100 MPa. During the

experiments, the effect of chemical environment (decane vs. water), grain angularity (well-rounded vs. subrounded/subangular) and grain-size distribution (GSD; narrow vs. broad) on deformation behavior is studied. We aim to highlight systematic qualitative and quantitative differences between our results on sand and observations on cemented sandstones, by making a systematic comparison between high-pressure deformation of sand versus sandstone, with a special focus on microstructural controls, strain localization, and acoustic characteristics.

2. Experimental Methods

We performed two types of conventional triaxial experiments on fluid-saturated sand aggregates under room temperature conditions:

1. Two hydrostatic tests (OS-04 and OS-17) were done at P_c up to 55 and 105 MPa, respectively. Decane-saturated test OS-04 was performed at fixed confining pressure steps of 2.5 MPa, while during each step, the sample was allowed to reach a near-steady volumetric strain rate of $<10^{-6}$ s^{-1}. Water-saturated test OS-17 was performed at a fixed confining pressure step rate of 2.5 MPa per 10 min. Both experiments were performed on a grain-size batch of $350 \pm 50 \mu$m.
2. Sixteen triaxial deformation tests were done with applied confining pressures (P_c) in the range 10–45 MPa, at a constant axial strain rate ($\dot{\epsilon}$) of 10^{-5} s^{-1}. After ~5% axial strain, strain rate was cycled several times from 10^{-6} s^{-1} to 10^{-4} s^{-1}, to test the effect of strain rate on deformation. These tests were performed using three different grain-size batches (350 ± 50 μm, 340 ± 160 μm and 240 ± 60 μm).

The experiments were either performed using decane or water as pore fluid (pore-fluid pressure, $P_p = 5$ MPa), to test the effect of chemical environment on deformation behavior. A summary of the experiments, plus key parameters obtained during the tests, is presented in Tables 1 and 2.

2.1. Sample Material and Preparation

The sand used in 17 of the experiments was ASTM standard C778 Ottawa sand obtained from U.S. Silica (Ottawa, IL, USA). Specifications indicated a SiO_2 content of 99.7 wt%, with minor quantities of Al_2O_3 (0.06 wt%), Fe_2O_3 (0.02 wt%), and TiO_2 (0.01 wt%). Scanning electron microscopy showed that most sand grains are well rounded, with smooth surfaces characterized by pressure solution indentations and quartz overgrowths. Fractions of the sand (350 ± 50 μm, 340 ± 160 μm, and 240 ± 60 μm) were prepared by sieving twice the material as received. Additionally, one experiment was performed using Beaujean sand, the same as used by Brzesowsky et al. (2011), Brzesowsky, Hangx, et al. (2014), and Brzesowsky, Spiers, et al. (2014). This material was obtained from the Heksenberg Formation, Beaujean quarry, Heerlen, Netherlands, and sieved to a grain-size fraction of 240 ± 60 μm. Compared to Ottawa sand, the Beaujean sand is more subrounded to subangular.

Prepacked sand aggregates (40 mm diameter, 100 mm length) were prepared by pouring a fixed amount of sand (~250 g in mass) into a Viton sample jacket used for the experiments (see Figure 1), followed by 10 min on a shaking plate with a small weight applied to the sand pack. Starting porosity was calculated using the exact sample dimensions and sample mass, assuming a density of quartz of 2.66 g/cm^3. This preparation method resulted in a well-controlled starting porosity within the range 36.0–36.3% for the Ottawa grain-size fraction of 300–400 μm (Table 1). Note that sample OS-06 had a slightly lower initial porosity of 34.6%, which could affect its mechanical behavior (Brzesowsky, Spiers, et al., 2014).

2.2. Experimental Apparatus and Procedure

The deformation experiments were performed in a conventional triaxial apparatus at the Rock and Ice Physics Laboratory of University College London (see description in Brantut et al., 2014; Eccles et al., 2005). The machine consists of an oil-filled pressure vessel, with servo-controlled application of axial load and pore pressure and manual application of confining pressure. After filling of the vessel, confining pressure on the sample was ~5 MPa. Confining and pore pressures were then increased in 1 MPa steps, such that the pore pressure never exceeded the confining pressure, up to 10 MPa confining pressure and 5 MPa pore pressure. Subsequently, only confining pressure was increased in 5 MPa steps to the target conditions. The sample was then left to equilibrate for about 2 hr. Axial shortening was measured using the average of two linear variable differential transformers, located outside of the pressure vessel, and used to calculate axial strain. All tests were performed under drained, constant pore pressure conditions. After ~5% axial strain, strain rate-stepping stages were performed by down-stepping the strain rate by one order of magnitude ($\dot{\epsilon} = 10^{-6}$

Table 1
Conventional Triaxial Compression and Hydrostatic Experiments Performed on Fluid-Saturated Ottawa Sand Aggregates (d = 300–400 μm) at 20 ° C and P_p = 5 MPa, Plus Unloading Young's Modulus Obtained in the Tests

Sample	ϕ_0 (%)	ϕ_i[a] (%)	P_c^{eff} (MPa)	E_u (GPa)	d_{50} (μm)
Starting material					427–444
Decane-saturated sand aggregates					
OS-03	36.3	33.6	20	6.3	351–375
OS-05	36.2	33.5	25	6.8	351–353
OS-02	36.0	32.6	30	7.8	318–339
OS-04[b]	36.1	36.1[c]	5–50		410–427
Water-saturated sand aggregates					
OS-15	36.3	36.3[c]	5	3.6	
OS-16[d]	36.2		10	4.5	438–439
OS-08	36.1	34.7	15		364–374
OS-11[e]	36.3	34.3	20	5.7	
OS-09[f]	36.1	34.0	20	5.4	
OS-06	34.6	32.9	20	5.9	
OS-12	36.0	33.9	20	6.5	374–386
OS-07	36.3	33.8	25	6.7	
OS-10	36.2	32.7	30	7.3	300
OS-18	36.3	31.1	40	8.1	
OS-17[b]	36.3	36.3[c]	5–100		

Note. Additionally, mean grain-size values are given when measured. Symbols: ϕ_0 is sample porosity prior to setup, ϕ_i is the estimated sample porosity after application of P_c and P_p, P_c^{eff} represents effective confining pressure, E_u is the Young's modulus obtained from a linear fit to the linear (elastic) part of the stress-strain curve during unloading, and d_{50} is the mean grain size obtained from particle size analysis (two measurements).
[a] The estimated porosity after application of confinement does not include any sample volume changes during the pore pressure application phase. Error is ~0.6% (see Appendix A). [b] Hydrostatic experiments: OS-04 performed at P_c steps of 2.5 MPa, while during each step, the sample was allowed to reach a near-steady volumetric strain rate of $< 10^{-6}$ s^{-1}. OS-17 performed at a fixed confining pressure step rate of 2.5 MPa per 10 min. [c] Experiment started immediately after application of the pore pressure (P_c^{eff} = 5 MPa). [d] Sample experienced jacket leakage, so no pore volume changes could be obtained. [e] Sample deformed up to 1.5%e. [f] Sample deformed up to 4%e.

s^{-1}), followed by up-stepping the strain rate by one order of magnitude compared to the initial strain rate ($\dot{\epsilon} = 10^{-4}$ s^{-1}). This sequence was repeated.

For all experiments, total axial strains of ~7.5% were achieved. Pore volume changes were determined by measuring the change in pore-fluid volume during deformation, as determined from the position of the actuator inside the servo-controlled pore pressure intensifier. The triaxial deformation experiments were terminated by halting the loading ram. Subsequently, the sample was unloaded at a strain rate of 10^{-5} s^{-1}, followed by reducing the confining and pore pressures to room pressure, making sure that at all times $P_c > P_p$.

2.3. Wave Velocity and Acoustic Emission Measurements

During deformation, acoustic emissions (AEs) and the evolution of *P*-wave velocities with increasing deformation were monitored. The sample jacket is equipped with 16 piezoelectric transducers positioned around, and directly touching, the sample and connected to 40 dB high-frequency preamplifiers and a 50 MHz digital recording system (e.g., Brantut et al., 2014; Figure 1). *P*-wave velocities were determined by regularly and sequentially sending a high-frequency (1 MHz) and high-voltage (250 V) pulse on each transducer

Table 2

Conventional Triaxial Compression Experiments Performed on Fluid-Saturated Aggregates of Ottawa and Beaujean Sand, With Different Grain Angularities and GSDs, at 20 ° C and P_p = 5 MPa, Plus Unloading Young's Modulus Obtained in the Tests

Sample	Sand type	d	ϕ_0	ϕ_i	E_u	d_{50}
		(μm)	(%)	(%)	(GPa)	(μm)
Effect of grain angularity: decane-saturated sand aggregates						
OS starting material						308–309
BS starting material						294–298
OS-19	Ottawa	180–300	37.4	30.9	8.0	280–283
	(well rounded)					
BS-01	Beaujean	180–300	38.6	31.6	8.0	198–227
	(subrounded/subangular)					
Effect of grain-size distribution: water-saturated sand aggregates						
Starting material (narrow)						308–309
Starting material (broad)						403–450
OS-07	Ottawa	300–400	36.3	33.8	6.7	
	(narrow GSD)					
OS-14	Ottawa	180–500	34.9	32.5	5.5	308–335
	(broad GSD)					

Note. GSD = grain-size distribution. Additionally, mean grain-size values are given when measured. Symbols: d is grain size, ϕ_0 is sample porosity prior to setup, ϕ_i is sample porosity after application of P_c and P_p, P_c^{eff} represents effective confining pressure, E_u is the Young's modulus obtained from a linear fit to the linear (elastic) part of the stress-strain curve during unloading, and d_{50} is the mean grain size obtained from particle-size analysis (two measurements).

while recording transmitted waves on the remaining sensors. During the time intervals between active wave velocity measurements, we monitored AE activity and recorded incoming signals when a threshold voltage (typically about 100 mV) was detected over five sensors. In addition to wave velocity and triggered AE waveform data, we also monitored the total of AE hits on each individual sensor, with time bins of 5 s.

2.4. Data Processing

External axial load, piston displacement, confining pressure, sample temperature, pore-fluid pressure, and pore-fluid volume change signals were logged at time intervals of 1 s. The raw data were processed to give differential stress ($\sigma_1 - \sigma_3$), axial strain (ϵ), axial strain rate ($\dot{\epsilon}$), and porosity change ($\Delta\phi$) data versus time. The displacement data were corrected for apparatus distortion using predetermined stiffness calibrations. The change in pore volume was used to calculate porosity change, assuming rigid solid particles.

Using a cross-correlation technique, precise *P*-wave arrival times were determined (for details, see Brantut et al., 2014). Assuming that volumetric deformation was uniformly distributed along the sample axis, the sensor positions were corrected from the axial and radial deformation achieved in each experiment. The local positions of the transducers around the sample allow for *P*-wave speeds to be calculated in four directions relative to the sample axis: 90.0°, 58.0°, 38.7°, and 28.1°, respectively. AEs were located using the arrival times of waveforms to the 16 transducers, assuming a homogenized transversely isotropic *P*-wave speed model that uses *P*-wave speeds interpolated in time from the measured values. Due to severe clipping of the wave form, it was not possible to assess the cumulative AE energy.

2.5. Microstructural Methods

After the experiments, the jacketed samples were extracted from the pressure vessel. Due to the friable nature of the sand aggregate, intact extraction of the sample was only possible by freezing the sample at −20 ° C for ~12 hr, while inside the jacket. The frozen sand aggregate was subsequently removed from the sample sleeve and emplaced in a fluorinated ethylene propylene (FEP) jacket of the same dimensions as the frozen sample. The samples were allowed to defrost and dry in an oven at 80 ° C for several weeks, prior to impregnation with LR white epoxy resin. Subsequently, thin sections were made from the material, roughly at the center of the aggregate, parallel to the compression axis. Though the samples were impregnated, they remained friable, and during thin section preparation, some grains were plucked from the section.
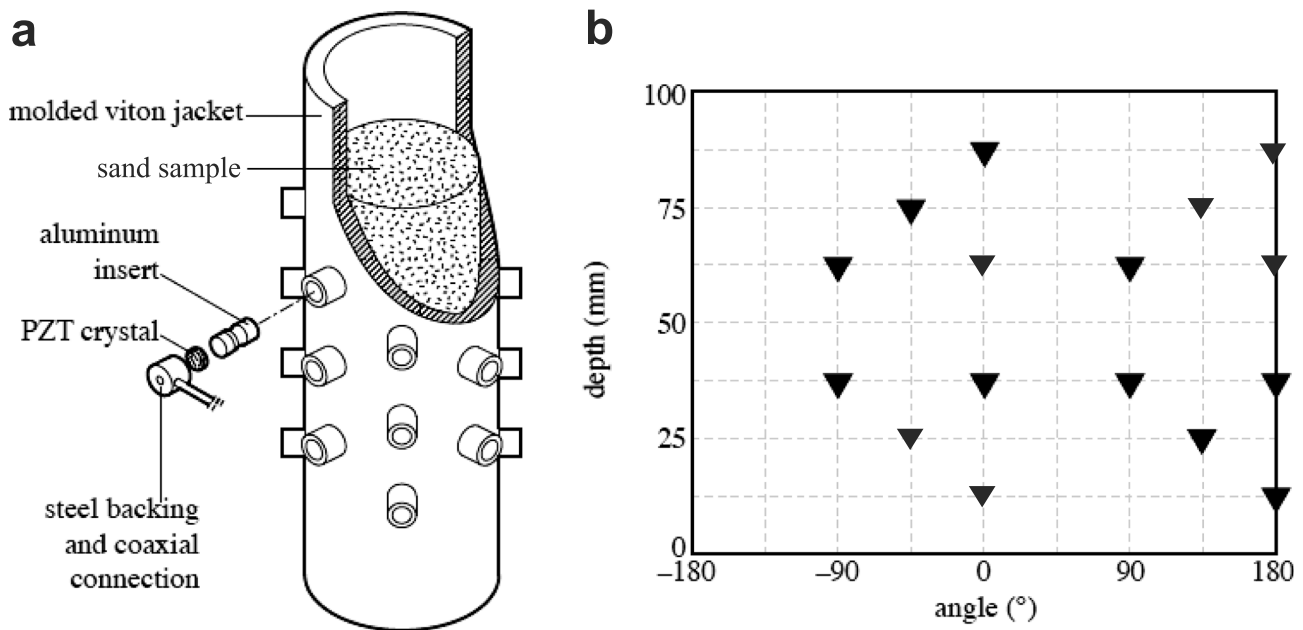
Figure 1. (a) Schematic of the sample (diameter is 40 mm, and length is 100 mm) and sample jacket. In total 16 acoustic transducers, containing lead zirconate titanate (PZT) crystals, were mounted on molded inserts in the jacket. Unused inserts were blanked with aluminum plugs. (b) Map of sensor positions around the sample.

Using an optical microscope, micrographs of approximately 10 by 10 mm were made. The freezing procedure did not seem to have affected the microstructure, as many grains and their associated grain fragments appear to be undisturbed. From these micrographs, crack maps were constructed (see Figure 2) by manually tracing all through-going or partially through-going cracks visible within the sand grains. Small cracks along grain edges, caused by chipping, were not mapped. The resulting crack maps were overlain by a grid of 100-μm spacing. Within a square of four cells, the number of cracks was counted and attributed to the center of the square. Each new square was shifted one cell (quadrant) with respect to the previous one (analogous to a Kalsbeek counting net; Kalsbeek, 1963). The resulting columns and rows of numbers were converted to a crack density contour map.

Due to the low freezing temperature of decane ($-30°$ C) it was not possible to freeze the decane-saturated samples, following the same method. Therefore, no attempts were made to preserve the microstructures of the decane-filled samples, and the sand was simply allowed to dry after removal from the sample sleeve. Loose sand grains from such experiments were examined using scanning electron microscopy, by mounting the powder on double-sided carbon tape on stubs.

Undeformed starting material and selected, postdeformation sand samples were analyzed using a Malvern laser particle sizer, to determine changes in the average grain-size (d_{50}) and GSD of each sample due to deformation. Prior to sampling, each material was well mixed, and a 0.5 g sample was taken for particle analysis. Agglomeration effects can appear to lead to Malvern particle-size analysis overestimating the mean grain size by up to ~1.5 times (Hangx et al., 2010), as well as to postexperiment distributions with grain sizes that are larger than those observed in the starting material. However, compared to grain-size analysis via optical methods, this method provides the opportunity to sample a larger number of grains, plus circumvents any stereological uncertainty obtained from 2-D thin section analysis.

3. Results
3.1. Fluid-Saturated Ottawa Sand Experiments: Effect of Chemical Environment
3.1.1. Mechanical Data
In this paper, we adopt the convention that compressive stresses, compressive axial strains, and porosity change are measured positive. The principal compressive stresses are denoted as σ_i, with $\sigma_1 > \sigma_2 = \sigma_3 = P_c$. The effective principal stresses are denoted σ_i^{eff} and are defined as $\sigma_i^{eff} = \sigma_i - P_p$, where P_p is pore pressure. Porosity changes during each experiment are measured from the point that pore-fluid pressure is applied
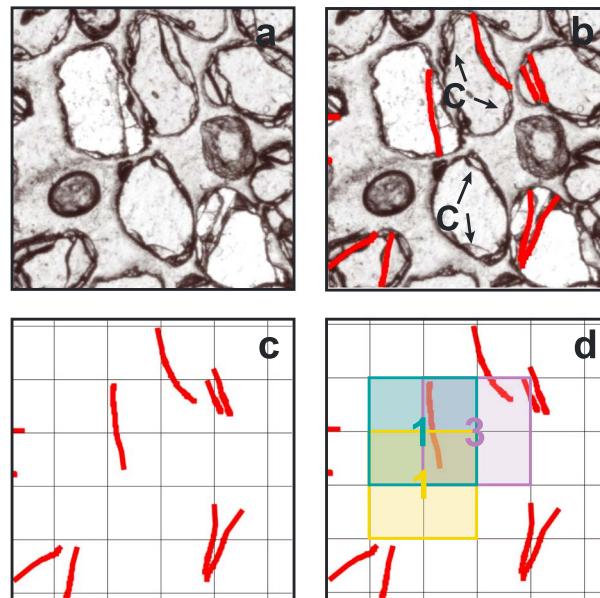
Figure 2. Procedure for processing of the microstructures to produce crack density contour maps. (a) Optical micrograph of a portion of a typical sand microstructure. (b) Cracks are marked in red, while chipping-related cracks (C) are not taken into account. (c) The crack map is overlain by a grid of 100 μm spacing. (d) Within squares of four grid cells, the number of cracks is counted and attributed to the center of the square. The resulting columns and rows are converted to a crack density contour map.

($P_c^{\text{eff}} = 5$ MPa). Note that no porosity change can be measured for the increase in effective confining pressure to 5 MPa, as up to that point the sample is dry. Extrapolation of porosity-P_c^{eff} data obtained during the hydrostatic stage (shown in Figure A1; see Appendix A) predicts that neglecting the porosity change that will occur during the dry stage will lead to an overestimation of the actual sample porosity, or an underestimation of the porosity change, by ~0.6%, which is negligible compared to the total porosity change measured during the experiments ($\Delta\phi$ up to 10%).

Differential stress-axial strain and mean stress-porosity change curves for hydrostatic and triaxial deformation experiments at effective pressures P_c^{eff} of 5 to 40 MPa under decane- and water-saturated conditions (pore-fluid pressure, $P_p = 5$ MPa) are presented in Figure 3. Overall, all experiments show an initial stage of quasilinear stress-strain behavior (Figures 3a and 3b). Only at very low effective confining pressure ($P_c^{\text{eff}} = 5$ MPa; cf. OS-15, Figure 3d) dilation is observed, while at higher confinement the Ottawa sand aggregates compact. After ~1% strain, the stress-strain curves become nonlinear, and the samples transition from strain-neutral toward strain-hardening behavior with increasing effective confining pressure (cf. Figure 3b). More porosity change is achieved at higher confinement, reaching near-uniaxial compaction (i.e., $\Delta\phi \simeq \epsilon$) at effective confining pressures of 40 MPa. Note that the slightly lower porosity sample OS–06 showed also slightly lower differential stresses at the same amount of axial deformation (Figure 3e). Overall, little effect of pore-fluid chemistry (decane vs. water) is observed in terms of aggregate strength and volumetric behavior.

The hydrostats (cf. OS-04 and OS-17 in Figures 3c and 3d, respectively) show a slightly sigmoidal shape with an initial concave upward trend between mean stress and porosity change, becoming quasi-linear after approximately 2% porosity change and concave downward again after 5% porosity change. At an effective mean stress of 50 MPa, 5.7% and 4.9% porosity change is achieved for the decane- and water-saturated hydrostatic experiment, respectively. The decane hydrostat follows the volumetric behavior seen in the hydrostatic stages of the decane-saturated triaxial deformation experiments. While the water hydrostat follows the hydrostatic stages of the water-saturated triaxial experiments up to effective confining pressures of 25 MPa, it underestimates compaction at higher confinement (Figure 3b). This may be related to sample preparation or to the pressurization procedure employed during the hydrostatic experiment. It should be noted that within the pressure range tested, the hydrostatic experiments lack any significant inflection point, generally associated with the departure from elastic behavior and the onset of inelastic compaction (P^*; Zhang et al., 1990).
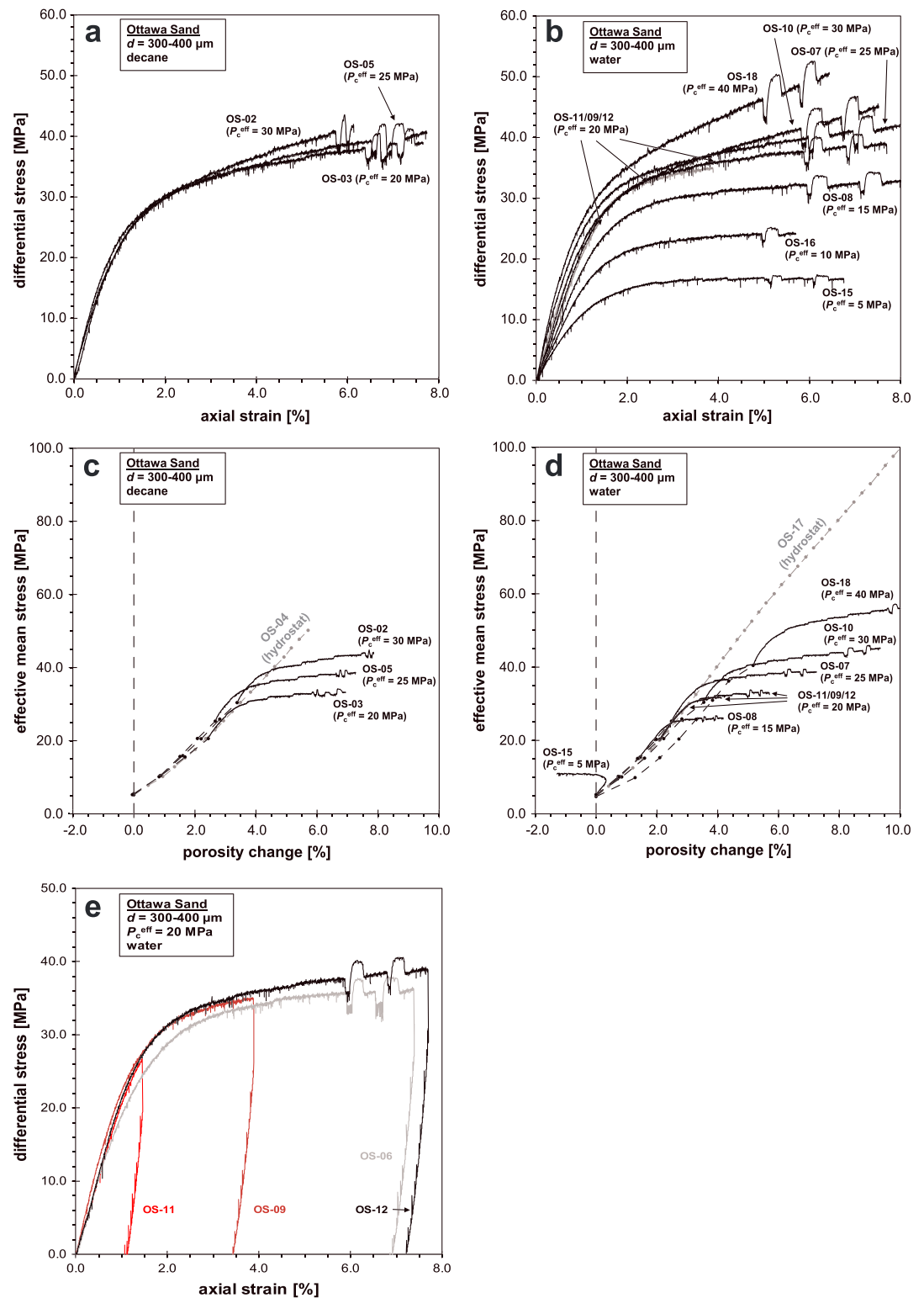
Figure 3. (a and b) Differential stress versus axial strain and (c and d) effective mean stress versus porosity change curves for triaxial experiments performed on decane-saturated and water-saturated Ottawa sand aggregates, at room temperature and fluid pressures of 5 MPa. Solid lines indicate triaxial deformation stages. Dotted lines show hydrostatic experiments or experiment stages. Strain rate-stepping stages resulted in up and down steps in differential (a and b) and mean stress (c and d) at the end of each experiment. (e) Differential stress versus axial strain curves for selected experiments, illustrating the experimental reproducibility, the impact of porosity on mechanical behavior (cf. OS-06 and OS-12) and typical unloading behavior.
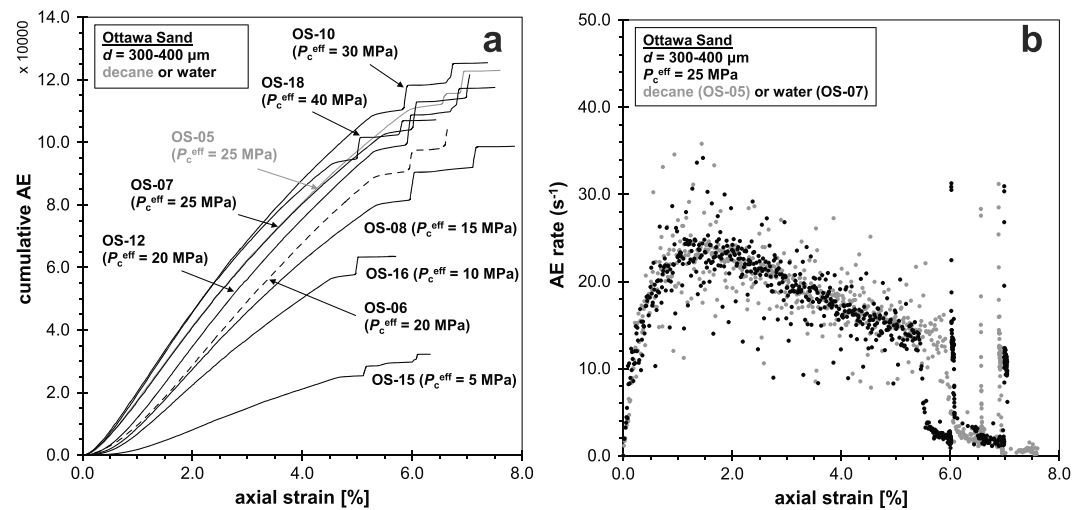
Figure 4. Acoustical data obtained for the decane- and water-saturated experiments ($d = 300 - 400 \mu$m). a) Cumulative AE and b) AE rate versus axial strain. Note that the strain rate-stepping stages were initiated after ~ 5 % axial strain.

In our triaxial deformation experiments, the nonlinearity of the stress-strain curves during loading makes the determination of a specific onset of inelastic behavior (commonly denoted C^* in sandstones - Wong et al., 1997) very elusive and was therefore not done. Upon unloading, the stress-strain data are near linear and show that 80–95% of the total axial strain is permanent deformation, at all stages of the experiment (Figure 3e). We use the linear portions of the unloading stress-strain curves to determine the apparent Young's Modulus (E_u; Zoback & Byerlee, 1975; Baud, Schubnel, et al., 2000; see Figure 3e; full data set available from the UK National Geoscience Data Centre). As reported in Table 1, Young's Modulus ranges from 3.6 to 8.1 GPa in the effective confining pressure range 5 to 40 MPa, increasing with P_c^{eff}. At constant confining pressure, E_u remains roughly constant throughout the experiment (cf. OS-11, OS-09, OS-06, and OS-12; Table 1 and Figure 3e). Pore-fluid does not affect the static elastic stiffness.

3.1.2. Acoustical Data

The evolution of the cumulative AE count and AE rates as a function of axial strain are shown in Figures 4a and 4b, respectively. For all experiments, cumulative AEs increase with increasing strain, showing concave upward behavior up to approximately 1% axial strain followed by concave downward behavior at larger deformation. Furthermore, more AEs are counted with increasing confining pressure. Note that for experiment OS-06, which had a slightly lower starting porosity, fewer cumulative AEs were counted during compaction.

AE rate, i.e. the time derivative of the cumulative AEs, shows a rapid initial increase in rate with axial strain, until it reaches a peak AE rate at an axial strain of ~1%, after which the rate slows down again. With increasing confining pressure, the peak AE rate increases in magnitude (~6.5 s^{-1} at 5 MPa P_c^{eff} to ~25 s^{-1} at P_c^{eff} >25 MPa) and occurs at lower axial strain with increasing confining pressure (~1.8 % at 5 MPa P_c^{eff} to ~1 % at P_c^{eff} >25 MPa). pore-fluid composition does not affect the cumulative number of AEs or the AE rate (cf. Figure 4b).

Absolute P-wave velocities during the decane- and water-saturated experiments, measured along the four wave paths, range from 1,800 to 2,250 m/s prior to deformation, increasing with increasing confinement, i.e. with decreasing porosity at the start of the triaxial deformation stage. The velocities measured through the lower half of the samples were consistently higher, most likely due to a slightly denser packing of the aggregate resulting from the preparation method. Changes in P-wave velocity with respect to the predeformation value are shown in Figure 5a as a function of axial strain for decane- and water-saturated sand ($P_c^{eff} = 20$ MPa). For all experiments, P-wave velocity increases rapidly for the initial 1–2% strain. At low confining pressure (P_c^{eff} <20 MPa), P-wave velocity decreases along all four wave paths and eventually becomes less than the starting value for the (sub)horizontal wave paths (58.0° and 90.0°). By contrast, at higher confining pressure, after the initial rapid increase, P-wave velocity stays constant or increases at a slower rate along the steeper wave paths (28.1° and 38.7°, and 58.0° at the highest P_c^{eff}). Upon unloading, P-wave velocity
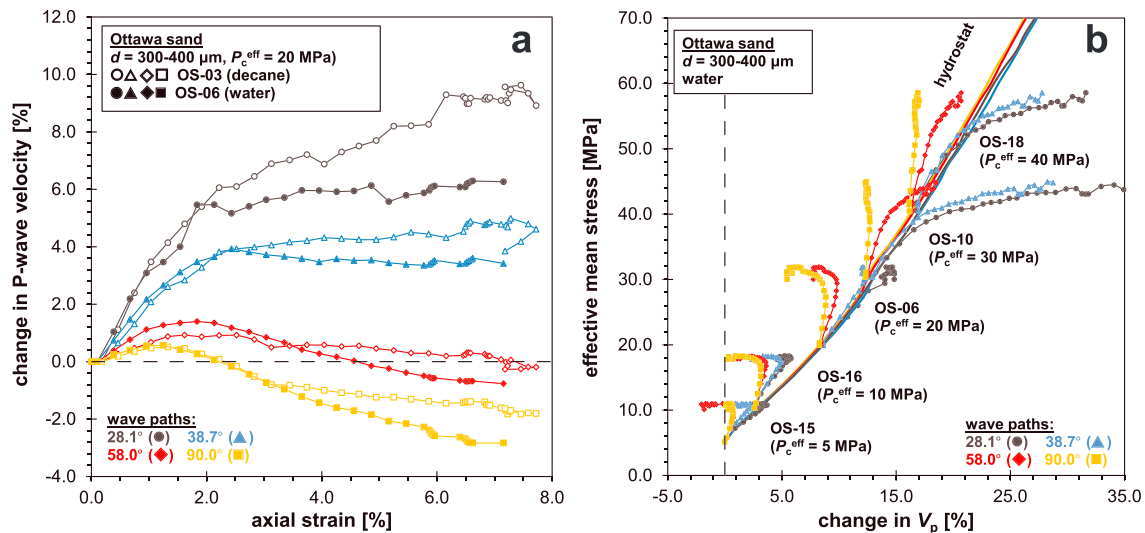
Figure 5. (a) Changes in *P*-wave velocity along the four wave path directions versus axial strain for experiments OS-03 (decane; open symbols) and OS-06 (water; closed symbols) at P_c^{eff} = 20 MPa. Strain rate stepping was initiated at ~5% axial strain. (b) Effective mean stress versus change in *P*-wave velocity at different effective confining pressures for water-saturated Ottawa sand aggregates. The triaxial deformation experiments are superimposed onto the hydrostat. Note that strain rate-stepping stages were initiated near the end of each experiment.

remains nearly constant for all experiments, suggesting that most of the measured deformation is permanent, in line with the mechanical data (cf. section 3.1.1). The evolution of V_p is not significantly affected by the pore-fluid type (Figure 5a).

For water-saturated aggregates, the evolution of *P*-wave velocity with effective mean stress, superimposed onto the hydrostat, is shown in Figure 5b. For the selected experiments, changes in *P*-wave velocity are shown along all four wave paths, to illustrate the development of azimuthal anisotropy of damage as a function of confining pressure. For all triaxial deformation experiments, the change in *P*-wave velocity initially increases linearly with effective mean stress and shows similar or slightly lower values compared to those measured under hydrostatic conditions. The initial rate of *P*-wave velocity increase is the lowest for the horizontal wave path, increasing as wave path angle rotates to subvertical, though no dependence on confinement is seen. As effective mean stress increases, *P*-wave velocity decreases with increasing mean stress along all wave paths for effective confining pressures up to 30 MPa. By contrast, at high confinement ($P_c^{\mathrm{eff}} \geq 30$ MPa) *P*-wave velocities increase rapidly with increasing stress, and thus strain, except along the horizontal wave path. The increase in wave velocity is most rapid in the subvertical direction, that is, subparallel to the compression direction. All experiments display an increase in wave-anisotropy (i.e., $V_p^{28.1°}/V_p^{90.0°}$) due to deformation, which becomes stronger with higher confinement (see Figure 5b). At low P_c^{eff}, anisotropy is slightly above one, at 1.05 to 1.1. As confining pressure increases to 30–40 MPa, anisotropy increases to 1.2–1.3.

3.1.3. Microstructural Analysis and Located AE Events

Undeformed Ottawa sand (d = 300–400 μm) consists of well-rounded grains with relative smooth surfaces (Figure 6a). After deformation, the grains have a more ragged appearance, most likely due to grain edge chipping such as seen in Figure 6b. Chipping is evident at low confinement (Figure 6b), where little grain crushing occurs. At higher confinement, fracturing and crushing becomes more dominant, shattering grains into angular fragments and small angular flakes (Figures 6c and 6d). These microstructural observations are confirmed by grain-size analyses (Figure 6e), which show the increased formation of finer particulates with increasing confinement. Very little grain-size reduction is observed in hydrostatic experiment OS-04 (decane), though compaction is following the same trend as the hydrostatic phases of the triaxial deformation experiments. No grain-size analysis could be performed on the water-saturated hydrostatic experiment (OS-17).

AE events indicate that localization at low confining pressure ($P_c^{\mathrm{eff}} \leq 5$ MPa) occurs along a shear plane. Though not evident from the microstructure, the volumetric data suggest that this plane is likely a dilation band. In line with this, pervasive grain failure is absent in the microstructure (Figure 6e), while grain edge
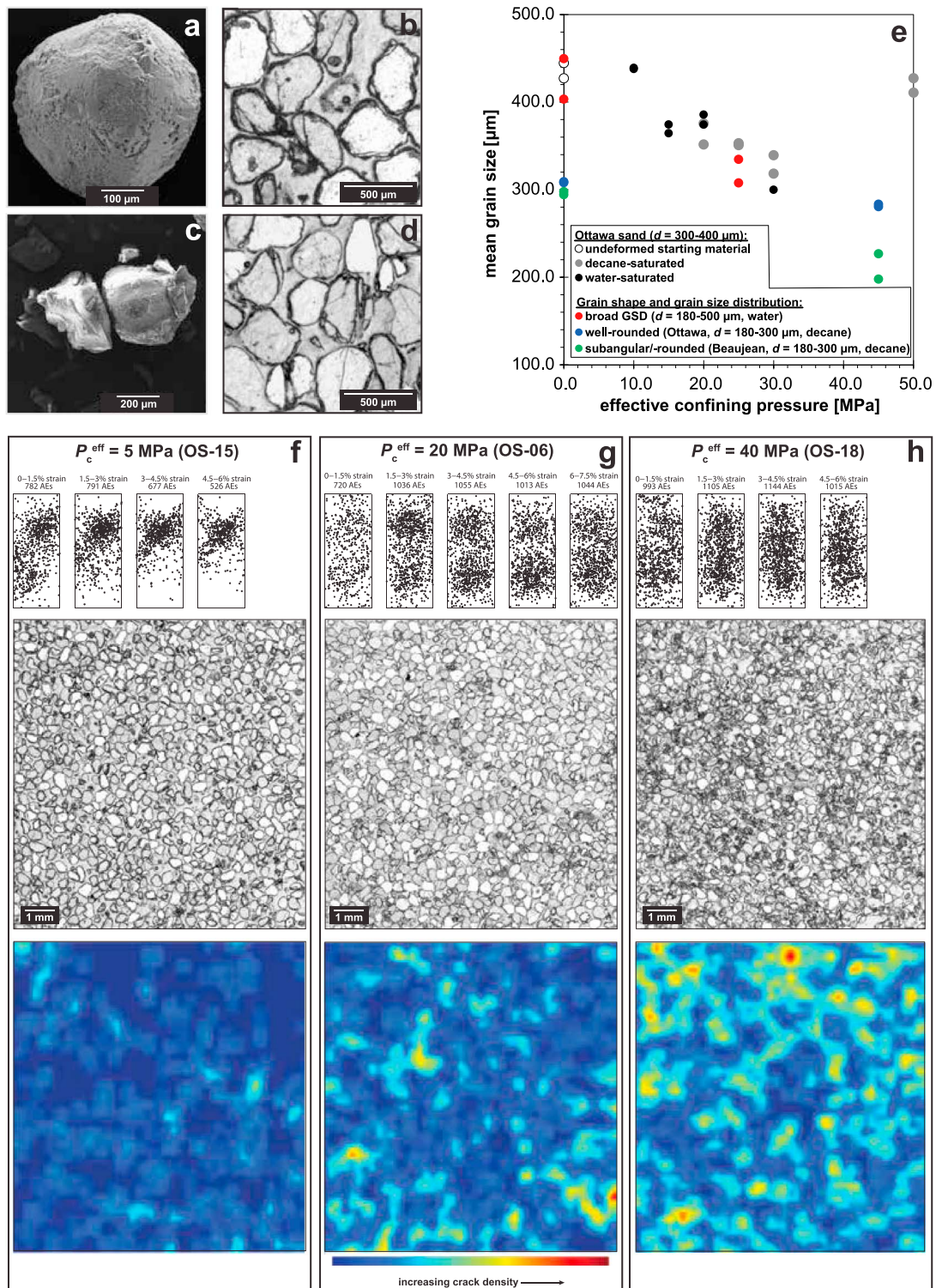
Figure 6. Scanning electron and optical micrographs of Ottawa sand grains, which are (a) undeformed, (b) compacted at low confining pressure (OS-15; $P_c^{eff} = 5$ MPa), and (c and d) compacted at high confining pressure (OS-12 [c] and OS-06 [d]; $P_c^{eff} = 20$ MPa). (e) Mean grain-size (d_{50}) versus confining pressure, showing a reduction in mean grain size with increasing confinement, indicative of the chipping and fracturing seen in (b)–(d). Located AE events for the whole sample (40 by 100 mm), optical micrographs of sections taken at the center of the sample (10 by 10 mm) and corresponding crack density contour maps obtained from water-saturated Ottawa sand aggregates, deformed at (e) 5 MPa (OS-15), (f) 20 MPa (OS-06), and (g) 40 MPa (OS-18) effective confining pressure. Note that the micrographs are not taken from the same slice through the sample as the AE locations.

chipping is prevalent, facilitating the required grain rotation and rearrangement needed for strain localization. At higher confining pressures ($P_c^{eff} \geq 10$ MPa) deformation appears to be more diffuse, with no clear indication of localization. Furthermore, the degree of grain fracturing and crushing increases with axial strain from 5.3 cracks per square millimeter at 1.5% strain (OS-09) to 5.6 cracks per square millimeter at 4.5% strain (OS-11) and 11.4 per square millimeter at 7.5% strain (OS-06; $P_c^{eff} = 20$ MPa), as well as with confining pressure (e.g., from 5.0 cracks per square millimeter at 5 MPa to 16.9 cracks per square millimeter at 40 MPa P_c^{eff}). The microstructures do not show clear indications for strain localization (cf. Figures 6f–6h).

3.2. Effect of Strain Rate

After ~5% axial strain, strain rate-stepping stages were performed by stepping the strain rate by one order of magnitude down and up. During strain rate down-steps, the differential stress, and hence also the mean stress, measured across the sample decreased. Similarly for strain up-steps, the differential and mean stress increased (cf. Figure 3). The magnitude of these stress changes appears to increase with increasing confining pressure.

The strain rate steps are also clearly reflected in the cumulative AE counts and AE rates. Decreasing the strain rate significantly reduces the AEs produced by the sample, down to a rate of <3 s^{-1}. Conversely, increasing the strain rate resulted in a rapid increase in the number of AEs, to a rate of ~30 s^{-1} (Figure 4). However, P-wave velocities are not significantly impacted by the strain rate-stepping sequence, which is in accordance with the observation that strain rate stepping does not affect sample volume changes.

### 3.3. Experiments Varying Grain Angularity and GSD

In addition to the experiments on well-rounded Ottawa sand with a narrow grain size, we also performed experiments on subrounded/subangular Beaujean sand ($d = 240 \pm 60$ μm) and Ottawa sand with a broader GSD ($d = 340 \pm 160$ μm). These experiments aimed at studying the effect of grain angularity (OS-19 and BS-01, $P_c^{eff} = 45$ MPa, decane) and GSD (OS-07 and OS-14, $P_c^{eff} = 25$ MPa, water) on compaction behavior (Table 2).

Differential stress-axial strain and porosity change-axial strain curves are presented in Figure 7. All four aggregates show behavior similar to the Ottawa sand described in section 3.1 with quasi-linear loading and near-uniaxial compaction behavior. All four experiments show significant strain hardening, which is more pronounced at high confining pressure. In terms of the effect of grain angularity, the mechanical data suggest that there is no significant difference in behavior between the well-rounded Ottawa sand and the more subrounded/subangular Beaujean sand. It is evident from Malvern grain-size analysis that the Beaujean sand underwent significant grain crushing, with d_{50} values reducing by ~28% from 296 to 212 μm (compared to only ~8% reduction for Ottawa sand, from 308 to 282 μm). Similarly, varying GSD, i.e. narrow versus broad, does not affect the mechanical behavior of the Ottawa sand aggregates. Microstructural observations show that the coarser grains within the aggregate remain largely intact during deformation, while the finer grains have been crushed (Figure 8). Compared to the narrow GSD Ottawa sand deformed at 25 MPa (OS-05), the average grain size has been significantly reduced, as a result of the formation of fines (d_{50} is 321 and 352 μm, respectively; see Figure 6e). No indications for strain localization are observed.

4. Discussion

4.1. Strain Localization

Preservation of deformation structures in sands is challenging due to the unconsolidated nature of the material. However, shear bands in sands have been recognized in nature (e.g., see Cashman & Cashman, 2000; Rawling & Goodwin, 2003) and in the laboratory (Alikarami et al., 2015). Structures seen in the Aztec sandstone are inferred to suggest that compaction bands may also form in unconsolidated sands (Sternlof et al., 2005), though to date no such laboratory observations have been made. By contrast, discrete compaction bands have been observed in sandstones in both nature (Mollema & Antonellini, 1996; Sternlof et al., 2006) and in the laboratory (see Wong & Baud, 2012, for an overview). While there may be differences in their characteristics, both natural and lab-induced compaction bands indeed show locally intense microcracking, grain comminution, and porosity reduction. However, not all sandstones are prone to compaction band formation. Porosity and rock homogeneity (mineralogy and GSD) play a significant role in controlling this type of strain localization (Cheung et al., 2012; Mollema & Antonellini, 1996), though their interplay is not yet well understood. Our results suggest that there is no evidence for compaction localization in unconsolidated sand deformed in the compactant regime.
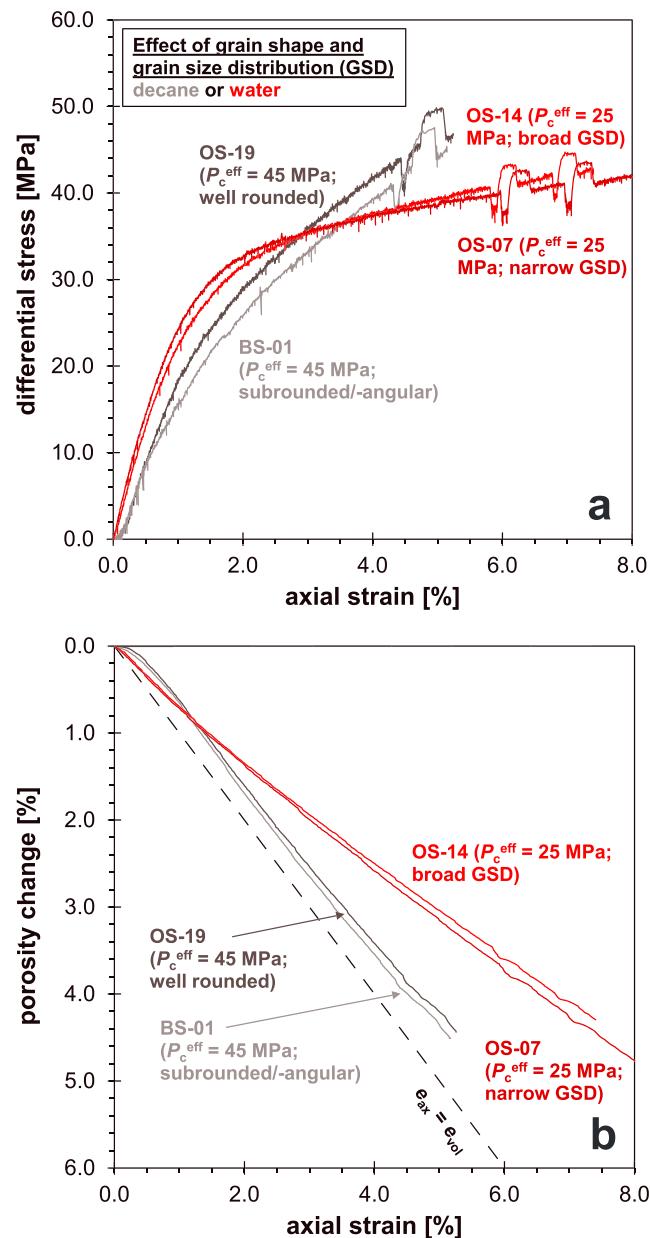
Figure 7. (a) Differential stress versus axial strain and (b) porosity change versus axial strain curves for triaxial experiments performed to test the effect of grain angularity (gray curves) and GSD (red curves) on mechanical behavior. Note that experiments OS-19 and BS-01 were performed on decane-saturated aggregates, while OS-07 and OS-14 were performed on water-saturated aggregates, at room temperature and fluid pressures of 5 MPa. Strain rate-stepping stages resulted in up and down steps in differential stress at the end of each experiment.

4.2. Effect of Water, Grain Angularity, and GSD On Behavior

In the presence of chemically active fluids like water, sandstones generally tend be significantly weaker (Baud, Zhu, et al., 2000; Baud et al., 2015; Duda & Renner, 2012; Tembe et al., 2008). Such physicochemical weakening of sandstones is attributed to the presence of altered feldspars and clay minerals (Baud, Zhu, et al., 2000), which reduce the proportion of strong, quartz-cemented grain-to-grain contacts. Furthermore, altered feldspars may promote crack nucleation and growth, while clays may promote slip through a reduction in frictional resistance when wet (Baud, Zhu, et al., 2000; Reviron et al., 2009). By contrast, very pure sandstones, like Fontainebleau and Bentheim sandstone, show no significant water weakening (Reviron et al., 2009; Tembe et al., 2008). Similarly, our experiments on decane- and water-saturated quartz sand ($d = 300 - 400$ μm) show no clear effect of a chemically active fluid on stress-strain and strain-V_p behavior,
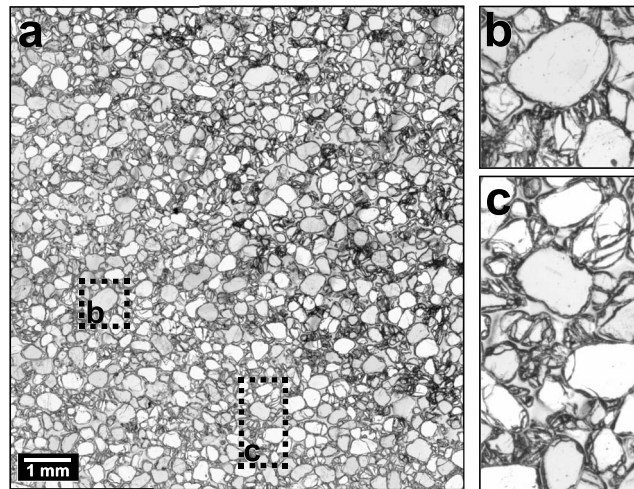
Figure 8. (a) Optical micrograph of Ottawa sand aggregates with a broad grain-size distribution ($d = 180$–500 μm), deformed at 25 MPa (OS-14), with (b) and (c) insets showing large surviving grains surrounded by crushed particles, suggesting shielding of the coarser grains by the finer grains present within the grain-size fraction.

and grain-size reduction within the range of strain rates investigated (cf. Figures 3, 5, and 6). These observations are in accordance with the behavior seen during time-independent uniaxial compaction of pure quartz sand, which is not significantly affected by chemical environment (Brzesowsky, Spiers, et al., 2014). This underpins the suggestion that the presence of other mineralogical phases is needed to promote water weakening. Recent work on impure sandstone inferred that intergranular slip at clay-coated grain boundaries may play an important role in controlling deformation, especially at stress conditions below the yield point (Pijnenburg et al., 2018, 2019).

Grain angularity is known to lead to sharper contact points and hence higher contact stresses, leading to more grain breakage (Chuhan et al., 2003; Zhang et al., 1990), i.e. the potential to create an instability. At the same time, in sandstones with a broad GSD, large grains tend to inhibit the propagation of instabilities, thereby hindering the formation of compaction bands (Cheung et al., 2012). We performed two experiments aimed at investigating the effect of grain angularity (Ottawa sand OS-19 vs. Beaujean sand BS-01, $P_c^{\text{eff}} = 45$ MPa, decane). Previous triaxial experiments on Ottawa and Hostun sand under lower confining conditions ($P_c = 0.1 - 7$ MPa; see Alikarami et al., 2015) showed comparable stress-strain behavior for the two sands, though the angular Hostun sand displayed more pronounced dilatation and grain breakage. While our experiments are performed at higher confining pressure conditions, we also observe very similar stress-strain behavior between the Ottawa and Beaujean sand. Furthermore, the more angular Beaujean sand shows significant grain failure and a smaller average grain size compared to the rounded Ottawa sand. We speculate that the more angular Beaujean sand has a higher tendency to strong interlocking, which would require the "chipping off" of larger fragments to unlock the aggregate and promote grain rearrangement, compared to the smoother, well-rounded Ottawa sand grains.

It should also be noted that overall finer-grained Ottawa sand ($d = 180$–300 μm) showed less grain-size reduction than coarser-grained Ottawa sand ($d = 300$–400 μm), even when deformed at higher effective confining pressure. This is inferred to be related to the tendency for larger grains to have a lower yield stress, making them more prone to grain failure (Chuhan et al., 2003; Zhang et al., 1990). Regarding GSD, stress-strain behavior is very comparable between the two end-members (OS-07 vs. OS-14, $P_c^{\text{eff}} = 25$ MPa, water). Looking at the microstructures, the broad GSD experiment displays shielding of the larger grains by the smaller grains, leading to less breakage of the coarser grains, supporting the observations made for Boise sandstone (Cheung et al., 2012). Overall, our experiments on Ottawa sand show that in terms of chemical environment, grain angularity and GSD, sands tend to show qualitatively similar behavior compared to sandstones.

4.3. Hardening Envelopes for Sand in PQ-Space
For sandstones, the yield point is typically defined as the stress conditions at which the material is no longer behaving poro-elastically (Wong & Baud, 2012). This point is generally accompanied with a marked increase
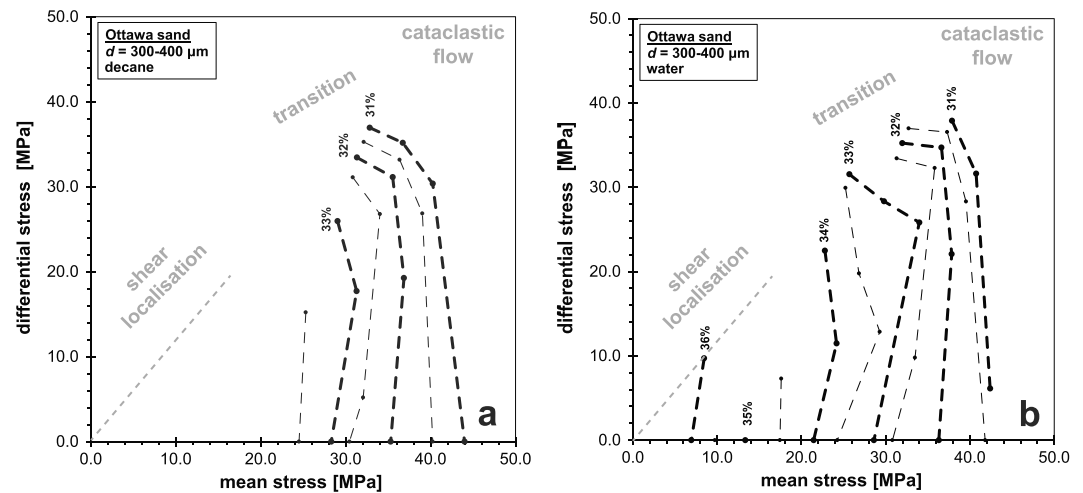
Figure 9. Hardening envelopes for specific aggregate porosity values plotted in differential stress versus mean stress space for (a) decane-saturated and (b) water-saturated Ottawa sand ($d = 300$–400μm) aggregates, at room temperature and fluid pressures of 5 MPa. Thick and thin dashed black lines separate porosity changes of 0.5%.

in AE activity (e.g., Fortin et al., 2006; Tembe et al., 2007). However, in the case of unconsolidated sand, large permanent deformation is seen during loading from the onset and elastic behavior is only observed upon unloading (Figure 3e). As such, no clear yield point can be pinpointed on the basis of the mechanical data, the AE activity or the P-wave velocities (cf. Figures 3b, 4a, and 5b). Therefore, to generate a meaningful description of the deformation behavior of this material, we propose it is more appropriate to represent the stress-strain data in terms of expanding hardening envelopes, each representing the stress supported at a specific porosity value. Since the sand aggregates continuously compact, this means that the hardening envelopes gradually grow as aggregate porosity decreases (Karner et al., 2005). A single loading path through these hardening envelopes then gives the stress-strain behavior of the material. As the mechanical behavior of Ottawa sand is reproducible and its material properties are near-constant throughout each experiment, delineating the mechanical behavior in terms of hardening envelopes is warranted (cf. compare OS-09, −11 and −12; see Table 1 and Figure 3e). For both the decane- and water-saturated aggregates, these hardening envelopes are drawn in differential stress, $Q = (\sigma_1 - \sigma_3)$, versus mean stress, $P = (\sigma_1 + 2\sigma_3)/3 - P_\mathrm{p}$, space (Figure 9).

As is clear from the hardening envelopes, Ottawa sand shows significant porosity reduction during the hydrostatic stage of the experiment (up to ∼5% at 40 MPa $P_\mathrm{c}^\mathrm{eff}$; cf. Figure 3), which has also been observed for St. Peter sand (Karner et al., 2003). However, the most striking feature of the contours is that they are near vertical up to ∼30 MPa differential stress, suggesting that porosity change is mainly controlled by mean stress, and not significantly by differential stress. Similar behavior has been observed before in St. Peter sand aggregates (Karner et al., 2005), porous bassanite (Bedford et al., 2018), and even in some highly porous sandstones (Pijnenburg et al., 2019; Tembe et al., 2007).

In essence, the hardening envelope for sand appears to consist of three linear parts: a shear failure line at low P, a narrow mean stress range during which deformation appears to be pressure insensitive, followed by a rapid transition to a near-vertical end cap, which increases in size as porosity decreases (see Figure 9). The bifurcation analysis of Issen and Rudnicki (2000) predicts that localized compaction bands form when the sum of the dilatancy factor β (the ratio of inelastic volumetric over shear strain increments) and friction parameter μ is $(\beta + \mu) < -\sqrt{3}$. Analysis of our data to tease out these constitutive parameters (see Table 3) suggests that at least in the highest confining pressure experiments conditions were favorable to promote compaction band formation. However, this prediction is at odds with our observations. Such a discrepancy between the prediction from bifurcation theory and experimental observations is not uncommon for sandstones and is likely due to the inadequacy of the constitutive description (Baud et al., 2006). Furthermore, it should be noted that we do not have access to the yield envelope sensu stricto, but to hardening envelopes, which might develop a different slope from the conventional yield envelope. This also inhibits a meaningful

Table 3

Constitutive Parameters Obtained for Conventional Triaxial Compression Experiments Performed on Water-Saturated Ottawa Sand Aggregates (d = 300–400 μm) at 20° C and P_p = 5 MPa

Sample	P_c^{eff} (MPa)	$\beta_{33\%}$ (−)	$\mu_{33\%}$ (−)	$h_{tan, 33\%}$ (GPa)	$\beta_{32\%}$ (−)	$\mu_{32\%}$ (−)	$h_{tan, 32\%}$ (GPa)	$\beta_{31\%}$ (−)	$\mu_{31\%}$ (−)	$h_{tan, 31\%}$ (GPa)
OS-08	15	0.13	1.83	0.01	0.19	0.67	0.10			
OS-09[a]	20	0.23	0.86	0.80	0.20	0.31	0.08			
OS-12	20	0.27	0.92	0.87	0.23	0.16	0.09			
OS-07	25	0.39	-0.30	1.19	0.30	-0.82	0.37	0.29	-1.02	0.09
OS-10	30	0.39	-0.30	1.19	0.38	-1.73	1.53	0.33	-1.93	0.47
OS-18	40							0.35	-12.11	3.88

Note. Symbols: P_c^{eff} represents effective confining pressure; β, μ, and h_{tan} are the constitutive parameters as needed for bifurcation analysis (Issen & Rudnicki, 2000; Rudnicki & Rice, 1975), obtained at sample porosities of 33%, 32%, and 31%, respectively. Here β is the dilatancy factor, μ is the internal friction coefficient, and h_{tan} is the tangent hardening modulus, obtained from the slope of a differential stress-axial strain plot (see Figure 3b).
[a] Sample deformed up to 4% e.

comparison between sand and sandstones. Given this discrepancy in behavior between sand and sandstone, the question now is as follows: What are the underlying microphysical processes controlling this behavior?

4.4. Mechanisms Driving Compaction and Potential for Strain Localization in Sands

In our lowest confinement experiment (P_c^{eff} = 5 MPa), we observed a dilating shear band, based on AE locations (cf. Figure 6f), similar to what is observed in Ottawa sand experiments under similar conditions using X-ray tomography imaging (Alikarami et al., 2015). However, no strain localization was observed at higher confinement. If strain localization had occurred, this would have been evident in the form of stress drops in the stress-strain behavior (Figure 3; Baud et al., 2004), or visible in the AE locations (Figures 6g and 6h; Fortin et al., 2006; Olsson & Holcomb, 2000), or crack density variations within the samples (crack density contour maps in Figure 6g-h; Baud et al., 2004; Fortin et al., 2006). Instead, under these conditions cataclastic flow appeared to control deformation, as also suggested by the near-vertical shape of our hardening envelopes (see section 4.3).

As summarized by Rudnicki (2007), compaction bands grow due to high stress concentrations at their tips. In other words, the failure of a grain should lead to the grain no longer supporting any stress and the subsequent redistribution of the stress to the surrounding grains; that is, it needs to lead to strain weakening/softening. Throughout all experiments, Ottawa sand shows near-strain-neutral to strain-hardening behavior (Figures 3a and 3b; Table 1). The progressive hardening of the material is also evidenced by the AE locations, which appear to propagate from the sample edge toward the center, and the continuously increasing P-wave velocities, suggesting a stronger, denser aggregate is being formed (cf. Figure 5). Therefore, the condition required for compaction band propagation, the creation of an instability, does not appear to occur.

Instead, we speculate that our data suggest that even at high confining pressure, grain-breakage, and concomitant grain rotation and rearrangement controls compaction. It is difficult to differentiate between AE events emerging from grain breakage and grain rotation (Wong et al., 1992), meaning that the AE locations could be derived from either (see Figures 6f–6h), as also suggested by Menéndez et al. (1996). However, significantly fewer AEs are observed at low confinement (Figure 4a), compared to high P_c^{eff} experiments. Microstructural evidence suggests that grain chipping (Figure 6b) is prevalent at these low confinement conditions, while progressively, more grain breakage occurs as confinement increases (see crack density contour maps in Figures 6f–6h).

This change in microstructural behavior with confining pressure is also suggested from the strain rate stepping data. As shown in Figures 10a and 10b, upon a change in axial strain rate, there is a change in differential stress supported by the sample. Overall, the differential stress change increases in magnitude when confining pressure increases, that is, when aggregate porosity goes down. Following Brantut et al. (2014), given that the strain rate is related to the differential stress as $\sigma^* \ln(\dot{\epsilon}/\dot{\epsilon}_0) \approx \Delta Q$, where σ^* is the activation stress, shows that at low P_c^{eff} (high porosity), the activation stress is very low (<0.5 MPa), while at higher confinement (lower porosity) the value is high (>1 MPa). High activation stresses are generally associated with
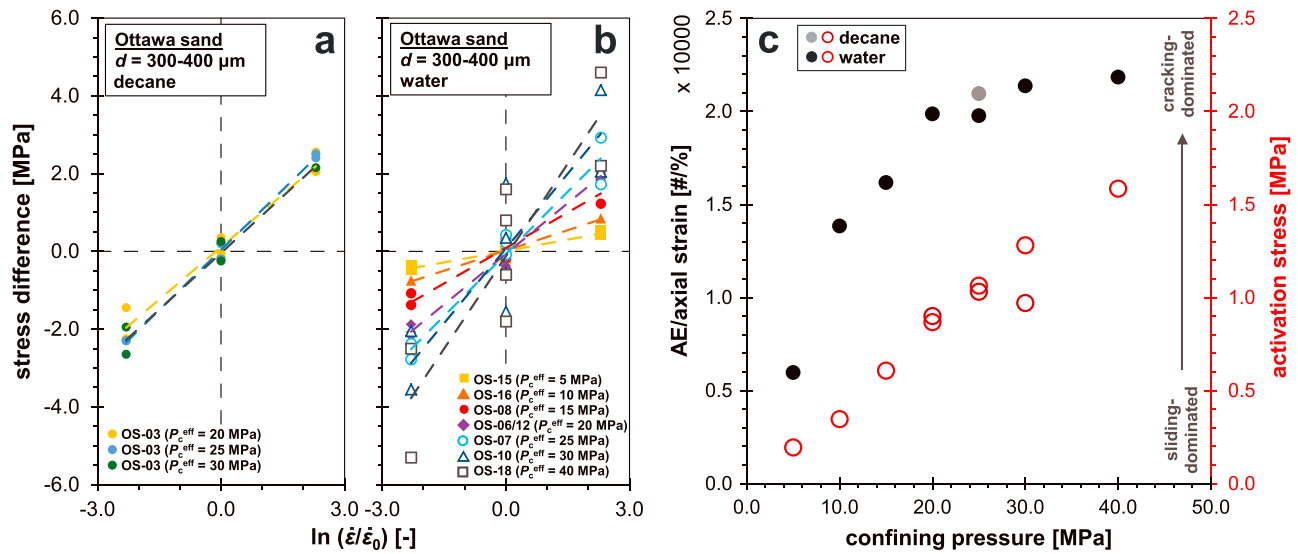
Figure 10. Differential stress difference measured upon a change in axial strain rate versus normalized strain rate for (a) decane-saturated and (b) water-saturated aggregates. (c) Cumulative number of acoustic emissions per unit axial strain and activation energy versus effective confining pressure for decane- and water-saturated aggregates.

cataclastic behavior in sandstones, for example, $\sigma^* = 4 - 5$ MPa for compaction band formation in Bleur-swiller sandstone (Heap et al., 2015). Similarly, looking at the cumulative AE data, we can see that fewer AEs are produced per unit axial strain at low confining pressure. The rate of AEs with unit axial strain (AE efficiency; see Wong et al., 1992) increases with confinement (Figure 10c). It has been suggested that this is generally associated with a transition from compaction by predominantly grain rotation/rearrangement, associated with minor grain fracturing (chipping), to predominantly grain failure plus grain rotation (Wong et al., 1992), in line with the observed strain rate dependency.

The above hypothesis for the grain-scale behavior is supported by the wave velocity data, which do not show significant changes in horizontal V_p, indicative of the opening of axial cracks. Furthermore, the decrease in P-wave velocities as failure approaches, such as observed for sandstones reflecting enhanced microcracking and pore collapse (Fortin et al., 2006), is also not observed. Though our samples experience significant grain failure, as evidenced by the grain-size and thin section analyses, the P-wave velocity appears not to be controlled by the formation of cracks. Instead, it is inferred that the data reflect that the acoustic behavior of Ottawa sand is associated with the contact area between grains (Digby, 1981; Walton, 1987).

Overall, we speculate that for our sand aggregates grain failure is easily accommodated by the rearrangement of surrounding grains, thereby preventing stress concentrations to arise within the aggregate. As the aggregate is subjected to higher confining pressures, it achieves a lower porosity and a more locked microstructure. Furthermore, higher confinement promotes more lateral constraint. So, while grain chipping is sufficient to promote rearrangement at low P_c^{eff}, grain crushing becomes more important at higher P_c^{eff}, as the grains experience less freedom to move around, as reflected in our microstructural, AE, and strain rate data. However, even at high confinement, grain rearrangement is still possible, meaning that no stress concentration, and hence no strain localization, will occur within the aggregate. The potential for compaction band formation therefore seems to be hinging on the degree of cementation at the grain contact, though it is unclear what the minimum degree of cementation should be and more research is needed on this (e.g., Bernabé et al., 1992; Yin & Dvorkin, 1994).

5. Conclusions

To probe the key differences between the mechanical behavior of unconsolidated sand and cemented porous sandstones, we performed systematic triaxial compression experiments on well-rounded Ottawa quartz sand at room temperature, strain rate of $10^{-6} - 10^{-4}$ s^{-1}, and effective confining pressures of 5–40 MPa. All samples had a well-controlled starting porosity of 36.0–36.3%, a narrow GSD (d = 300–400 μm) and were either decane (inert fluid) or water (chemically active fluid) saturated. Additionally, a limited number of

experiments were performed to assess the effect of grain angularity (Beaujean sand) and a broader GSD ($d = 180$–$500\,\mu m$) on behavior. The observed mechanical, acoustical, and microstructural behavior was compared to that seen in highly porous sandstones, in order to elucidate whether strain localization, in the form of shear and compaction bands, can occur in sands as well. We observed the following:

1. Pure quartz Ottawa sand initially shows quasi-linear stress-strain behavior going to strain-neutral and strain-hardening behavior with increasing effective confining pressure. Overall, only at very low P_c^{eff} (5 MPa) dilatant behavior is seen, while compacting increases with effective confining pressure. This behavior is also reflected in the P-wave velocities, with initial V_p values of 1,800–2,300 m/s that increase by up to 20 % as compaction progresses.

2. The presence of an inert or chemically active fluid did not significantly affect the mechanical and acoustical behavior of Ottawa sand. These observations are in line with what is observed for pure quartz sandstones.

3. Grain angularity and GSD also did not affect the stress-strain behavior of the sand. More angular Beaujean quartz sand shows more grain crushing, which is expected due to the presence of sharper grain-to-grain contacts, leading to higher contact stresses. For aggregates with a broader GSD, large grains tend to be shielded by smaller grains, which end up being crushed. Qualitatively, this behavior is also seen in sandstones, such as the Boise sandstone.

4. As our sand aggregates do not show truly elastic and yield behavior, the mechanical behavior is better described using hardening envelopes. In PQ-space, these hardening envelopes appear to consist of a linear shear failure line and a rapid transition to a near-vertical end cap. At low confining pressure, we see the formation of a dilation shear band, while at high confinement cataclastic flow dominates compaction behavior, in line with the behavior expected from the hardening envelopes. No compaction bands are observed.

5. The lack of cementation is inferred to lead to relatively easy grain rotation and rearrangement upon grain chipping and failure. As a result, no instability or strain localization can occur, which would lead to the formation of compaction bands. It is believed that cementation plays a key role in controlling strain localization via compaction bands, though it is unclear how exactly and more research is needed.

Appendix A: Sample Porosity After Hydrostatic Phase

Volumetric changes cannot be measured during the initial stage of the hydrostatic phase, up to $P_c = 5$ MPa, as no pore fluid is introduced into the sample yet, and hence, sample porosity cannot be calculated. After the introduction of pore fluid, the volumetric changes are measured during the subsequent application of hydrostatic pressure, which is used to calculate sample porosity. The dependence of starting porosity on confining pressure is shown in Figure A1.
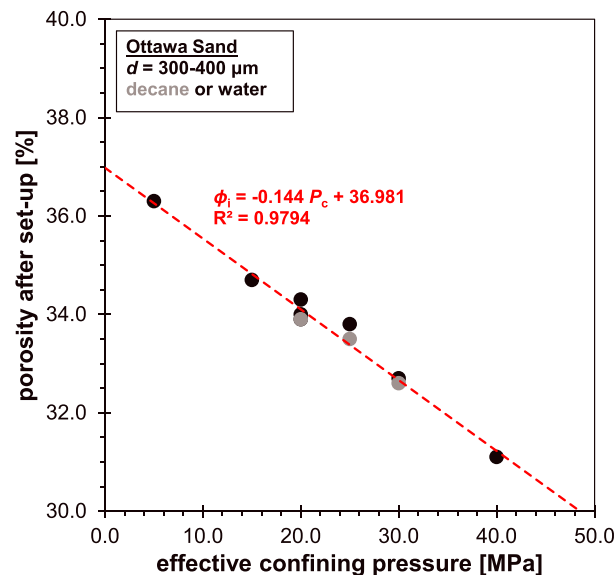
Figure A1. Porosity at the end of the hydrostatic setup phase as a function of effective confining pressure.

References

Alikarami, R., Andò, E., Gkiousas-Kapnisis, M., Torabi, A., & Viggiani, G. (2015). Strain localisation and grain breakage in sand under shearing at high mean stress: Insights from in situ X-ray tomography. *Acta Geotechnica*, *10*(1), 15–30. https://doi.org/10.1007/s11440-014-0364-6

Baud, P., Klein, E., & Wong, T.-F. (2004). Compaction localization in porous sandstones: Spatial evolution of damage and acoustic emission activity. *Journal of Structural Geology*, *26*(4), 603–624. https://doi.org/10.1016/j.jsg.2003.09.002

Baud, P., Reuschlé, T., Ji, Y., Cheung, C. S. N., & Wong, T.-F. (2015). Mechanical compaction and strain localization in Bleurswiller sandstone. *Journal of Geophysical Research: Solid Earth*, *120*, 6501–6522. https://doi.org/10.1002/2015JB012192

Baud, P., Schubnel, A., & Wong, T.-F. (2000). Dilatancy, compaction, and failure mode in Solnhofen limestone. *Journal of Geophysical Research*, *105*(B8), 19,289–19,303. https://doi.org/10.1029/2000JB900133

Baud, P., Vajdova, V., & Wong, T.-F. (2006). Shear-enhanced compaction and strain localization: Inelastic deformation and constitutive modeling of four porous sandstones. *Journal of Geophysical Research*, *111*, B12401. https://doi.org/10.1029/2005JB004101

Baud, P., Zhu, W., & Wong, T.-F. (2000). Failure mode and weakening effect of water on sandstone. *Journal of Geophysical Research*, *105*(B7), 16,371–16,389. https://doi.org/10.1029/2000JB900087

Bedford, J. D., Faulkner, D. R., Leclère, H., & Wheeler, J. (2018). High-resolution mapping of yield curve shape and evolution for porous rock: The effect of inelastic compaction on porous bassanite. *Journal of Geophysical Research: Solid Earth*, *123*, 1217–1234. https://doi.org/10.1002/2017JB015250

Bernabé, Y., Fryer, D. T., & Hayes, J. A. (1992). The effect of cement on the strength of granular rocks. *Geophysical Research Letters*, *19*(14), 1511–1514. https://doi.org/10.1029/92GL01288

Brantut, N., Heap, M. J., Baud, P., & Meredith, P. G. (2014). Rate- and strain-dependent brittle deformation of rocks. *Journal of Geophysical Research: Solid Earth*, *119*, 1818–1836. https://doi.org/10.1002/2013JB010448

Brzesowsky, R. H., Hangx, S. J. T., Brantut, N., & Spiers, C. J. (2014). Compaction creep of sands due to time-dependent grain failure: Effects of chemical environment, applied stress, and grain size. *Journal of Geophysical Research: Solid Earth*, *119*, 7521–7541. https://doi.org/10.1002/2014JB011277

Brzesowsky, R. H., Spiers, C. J., Peach, C. J., & Hangx, S. J. T. (2011). Failure behavior of single sand grains: Theory versus experiment. *Journal of Geophysical Research*, *116*, B06205. https://doi.org/10.1029/2010JB008120

Brzesowsky, R. H., Spiers, C. J., Peach, C. J., & Hangx, S. J. T. (2014). Time-independent compaction behavior of quartz sands. *Journal of Geophysical Research: Solid Earth*, *119*, 936–956. https://doi.org/10.1002/2013JB010444

Buscarnera, G., & Laverack, R. T. (2014). Path dependence of the potential for compaction banding: Theoretical predictions based on a plasticity model for porous rocks. *Journal of Geophysical Research: Solid Earth*, *119*, 1882–1903. https://doi.org/10.1002/2013JB010562

Cashman, S., & Cashman, K. (2000). Cataclasis and deformation-band formation in unconsolidated marine terrace sand, Humboldt County, California. *Geology*, *28*(2), 111. https://doi.org/10.1130/0091-7613(2000)28<111:CADFIU>2.0.CO;2

Cheung, C. S. N., Baud, P., & Wong, T.-F. (2012). Effect of grain size distribution on the development of compaction localization in porous sandstone. *Geophysical Research Letters*, *39*, l21302. https://doi.org/10.1029/2012GL053739

Choo, J., & Lee, S. (2018). Enriched galerkin finite elements for coupled poromechanics with local mass conservation. *Computer Methods in Applied Mechanics and Engineering*, *341*, 311–332. https://doi.org/10.1016/j.cma.2018.06.022

Chuhan, F. A., Kjeldstad, A., Bjørlykke, K., & Høeg, K. (2002). Porosity loss in sand by grain crushing experimental evidence and relevance to reservoir quality. *Marine and Petroleum Geology*, *19*(1), 39–53. https://doi.org/10.1016/S0264-8172(01)00049-6

Chuhan, F. A., Kjeldstad, A., Bjørlykke, K., & Høeg, K. (2003). Experimental compression of loose sands: Relevance to porosity reduction during burial in sedimentary basins. *Canadian Geotechnical Journal*, *40*(5), 995–1011. https://doi.org/10.1139/t03-050

Digby, P. J. (1981). The effective elastic moduli of porous granular rocks. *Journal of Applied Mechanics*, *48*(4), 803–808. https://doi.org/10.1115/1.3157738

Doornhof, D., Kristiansen, T., Nagel, N., Patillo, P., & Sayers, C. (2006). Compaction and subsidence. Oilfield Review, Autumn, 50–68.

Duda, M., & Renner, J. (2012). The weakening effect of water on the brittle failure strength of sandstone. *Geophysical Journal International*, *192*, 1091–1108. https://doi.org/10.1093/gji/ggs090

Eccles, D., Sammonds, P., & Clint, O. (2005). Laboratory studies of electrical potential during rock failure. *International Journal of Rock Mechanics and Mining Sciences*, *42*(7-8), 933–949. https://doi.org/10.1016/j.ijrmms.2005.05.018

Einav, I. (2007). Breakage mechanics part I: Theory. *Journal of the Mechanics and Physics of Solids*, *55*(6), 1274–1297. https://doi.org/10.1016/j.jmps.2006.11.003

Fawad, M., Mondol, N. H., Jahren, J., & Bjørlykke, K. (2011). Mechanical compaction and ultrasonic velocity of sands with different texture and mineralogical composition. *Geophysical Prospecting*, *59*(4), 697–720. https://doi.org/10.1111/j.1365-2478.2011.00951.x

Fortin, J., Guéguen, Y., & Schubnel, A. (2007). Effects of pore collapse and grain crushing on ultrasonic velocities and V_p/V_s. *Journal of Geophysical Research*, *112*, B08207. https://doi.org/10.1029/2005JB004005

Fortin, J., Stanchits, S., Dresen, G., & Guéguen, Y. (2006). Acoustic emission and velocities associated with the formation of compaction bands in sandstone. *Journal of Geophysical Research*, *111*, B10203. https://doi.org/10.1029/2005JB003854

Guo, P., & Xubin, S. (2007). Shear strength, interparticle locking, and dilatancy of granular materials. *Canadian Geotechnical Journal*, *44*(5), 579–591.

Hangx, S. J. T., Spiers, C. J., & Peach, C. J. (2010). Creep of simulated reservoir sands and coupled chemical-mechanical effects of CO_2 injection. *Journal of Geophysical Research*, *115*, B09205. https://doi.org/10.1029/2009JB006939

Heap, M. J., Brantut, N., Baud, P., & Meredith, P. G. (2015). Time-dependent compaction band formation in sandstone. *Journal of Geophysical Research: Solid Earth*, *120*, 4808–4830. https://doi.org/10.1002/2015JB012022

Hettema, M., Papamichos, E., & Schutjens, P. (2002). Subsidence différée: Observations et analyse à partir de données de champs. *Oil & Gas Science and Technology - Revue d'IFP*, *57*(5), 443–458. https://doi.org/10.2516/ogst:2002029

Issen, K. A., & Rudnicki, J. W. (2000). Conditions for compaction bands in porous rock. *Journal of Geophysical Research*, *105*(B9), 21,529–21,536.

Kalsbeek, F. (1963). A hexagonal net for the counting out and testing of fabric diagrams. *Neues Jahrbuch fur Mineralogie Monatshefte*, *7*, 173–176.

Karner, S. L., Chester, J. S., Chester, F. M., Kronenberg, A. K., & Hajash, A. (2005). Laboratory deformation of granular quartz sand: Implications for the burial of clastic rocks. *AAPG Bulletin*, *89*(5), 603–625. https://doi.org/10.1306/12200404010

Karner, S. L., Chester, F. M., Kronenberg, A. K., & Chester, J. S. (2003). Subcritical compaction and yielding of granular quartz sand. *Tectonophysics*, *377*(3), 357–381. https://doi.org/10.1016/j.tecto.2003.10.006

Klein, E., Baud, P., Reuschlé, T., & Wong, T.-F. (2001). Mechanical behaviour and failure mode of Bentheim sandstone under triaxial compression. *Physics and Chemistry of the Earth, Part A: Solid Earth and Geodesy*, *26*(1), 21–25. https://doi.org/10.1016/S1464-1895(01)00017-5

Lee, K. L., & Farhoomand, I. (1967). Compressibility and crushing of granular soil in anisotropic triaxial compression. *Canadian Geotechnical Journal*, *4*(1), 68–86. https://doi.org/10.1139/t67-012

Li, X., Mitchum, F., Bruno, M., Pattillo, P., & Willson, S. (2003). Compaction, subsidence, and associated casing damage and well failure assessment for the Gulf of Mexico Shelf Matagorda Island 623 Field. SPE Annual Technical Conference and Exhibition, Society of Petroleum Engineers.

Louis, L., Wong, T.-F., Baud, P., & Tembe, S. (2006). Imaging strain localization by X-ray computed tomography: Discrete compaction bands in Diemelstadt sandstone. *Journal of Structural Geology*, *28*(5), 762–775. https://doi.org/10.1016/j.jsg.2006.02.006

Marketos, G., & Bolton, M. (2009). Compaction bands simulated in discrete element models. *Journal of Structural Geology*, *31*(5), 479–490. https://doi.org/10.1016/j.jsg.2009.03.002

Menéndez, B., Zhu, W., & Wong, T.-F. (1996). Micromechanics of brittle faulting and cataclastic flow in Berea sandstone. *Journal of Structural Geology*, *18*(1), 1–16. https://doi.org/10.1016/0191-8141(95)00076-P

Mesri, G., & Vardhanabhuti, B. (2009). Compression of granular materials. *Canadian Geotechnical Journal*, *46*(4), 369–392. https://doi.org/10.1139/T08-123

Mollema, P., & Antonellini, M. (1996). Compaction bands: A structural analog for anti-mode I cracks in aeolian sandstone. *Tectonophysics*, *267*(1), 209–228. https://doi.org/10.1016/S0040-1951(96)00098-4

Muñoz-Ibáñez, A., Delgado-Martín, J., & Grande-García, E. (2019). Acoustic emission processes occurring during high-pressure sand compaction. *Geophysical Prospecting*, *67*(4), 761–783. https://doi.org/10.1111/1365-2478.12691

Nguyen, V., Gland, N., Dautriat, J., David, C., Wassermann, J., & Guélard, J. (2014). Compaction, permeability evolution and stress path effects in unconsolidated sand and weakly consolidated sandstone. *International Journal of Rock Mechanics and Mining Sciences*, *67*, 226–239. https://doi.org/10.1016/j.ijrmms.2013.07.001

Olsson, W. A., & Holcomb, D. J. (2000). Compaction localization in porous rock. *Geophysical Research Letters*, *27*(21), 3537–3540. https://doi.org/10.1029/2000GL011723

Olsson, W. A., Holcomb, D. J., & Rudnicki, J. W. (2002). Compaction localization in porous sandstone: Implications for reservoir mechanics. *Oil & Gas Science and Technology - Revue d'IFP*, *57*(5), 591–599. https://doi.org/10.2516/ogst:2002040

Ostermeier, R. (1995). Deepwater Gulf of Mexico turbidites—Compaction effects on porosity and permeability. *SPE Formation Evaluation*, *10*(2), 79–85. https://doi.org/10.2118/26468-PA

Pestana, J. M., & Whittle, A. J. (1999). Formulation of a unified constitutive model for clays and sands. *International Journal for Numerical and Analytical Methods in Geomechanics*, *23*(12), 1215–1243. https://doi.org/10.1002/(SICI)1096-9853(199910)23:12<1215::AID-NAG29>3.0.CO;2-F

Pestana, J. M., Whittle, A. J., & Salvati, L. A. (2002). Evaluation of a constitutive model for clays and sands: Part I sand behaviour. *International Journal for Numerical and Analytical Methods in Geomechanics*, *26*(11), 1097–1121. https://doi.org/10.1002/nag.237

Pijnenburg, R. P. J., Verberne, B. A. V., Hangx, S. J. T., & Spiers, C. J. (2018). Deformation behavior of sandstones from the seismogenic Groningen gas field: Role of inelastic versus elastic mechanisms. *Journal of Geophysical Research: Solid Earth*, *123*, 5532–5558. https://doi.org/10.1029/2018JB015673

Pijnenburg, R., Verberne, B., Hangx, S., & Spiers, C. (2019). Inelastic deformation of the Slochteren sandstone: Stress-strain relations and implications for induced seismicity in the Groningen gas field. *Journal of Geophysical Research: Solid Earth*, *124*, 1–29. https://doi.org/10.1029/2019JB017366

Potyondy, D., & Cundall, P. (2004). A bonded-particle model for rock. *International Journal of Rock Mechanics and Mining Sciences*, *41*(8), 1329–1364. https://doi.org/10.1016/j.ijrmms.2004.09.011, rock Mechanics Results from the Underground Research Laboratory, Canada.

Rawling, G. C., & Goodwin, L. B. (2003). Cataclasis and particulate flow in faulted, poorly lithified sediments. *Journal of Structural Geology*, *25*(3), 317–331. https://doi.org/10.1016/S0191-8141(02)00041-X

Reviron, N., Reuschlé, T., & Bernard, J.-D. (2009). *The brittle deformation regime of water-saturated siliceous sandstones, Geophysical Journal International*, *178*(3), 1766–1778. https://doi.org/10.1111/j.1365-246X.2009.04236.x

Rudnicki, J. W. (2007). Models for compaction band propagation. In C. David, & M. Le Ravalec-Dupin (Eds.), *Rock Physics and Geomechanics in the study of Reservoir and Repositories, Special Publications* (Vol. 284, pp. 107–125). London: Geological Society.

Rudnicki, J., & Rice, J. (1975). Conditions for the localization of deformation in pressure-sensitive dilatant materials. *Journal of the Mechanics and Physics of Solids*, *23*(6), 371–394. https://doi.org/10.1016/0022-5096(75)90001-0

Skurtveit, E., Torabi, A., Gabrielsen, R. H., & Zoback, M. D. (2013). Experimental investigation of deformation mechanisms during shear-enhanced compaction in poorly lithified sandstone and sand. *Journal of Geophysical Research: Solid Earth*, *118*, 4083–4100. https://doi.org/10.1002/jgrb.50342

Spetzler, J., & Dost, B. (2017). Hypocentre estimation of induced earthquakes in Groningen. *Geophysical Journal International*, *209*(1), 453–465. https://doi.org/10.1093/gji/ggx020

Sternlof, K. R., Karimi-Fard, M., Pollard, D. D., & Durlofsky, L. J. (2006). Flow and transport effects of compaction bands in sandstone at scales relevant to aquifer and reservoir management. *Water Resources Research*, *42*, W07425. https://doi.org/10.1029/2005WR004664

Sternlof, K. R., Rudnicki, J. W., & Pollard, D. D. (2005). Anticrack inclusion model for compaction bands in sandstone. *Journal of Geophysical Research*, *110*, B11403. https://doi.org/10.1029/2005JB003764

Tembe, S., Baud, P., & Wong, T.-F. (2008). Stress conditions for the propagation of discrete compaction bands in porous sandstone. *Journal of Geophysical Research*, *113*, B09409. https://doi.org/10.1029/2007JB005439

Tembe, S., Vajdova, V., Baud, P., Zhu, W., & Wong, T.-F. (2007). A new methodology to delineate the compactive yield cap of two porous sandstones under undrained condition. *Mechanics of Materials*, *39*(5), 513–523. https://doi.org/10.1016/j.mechmat.2006.08.005

Tengattini, A., Das, A., Nguyen, G. D., Viggiani, G., Hall, S., & Einav, I. (2014). A thermomechanical constitutive model for cemented granular materials with quantifiable internal variables. part i-theory. *Journal of the Mechanics and Physics of Solids*, *70*, 281–296.

Vesíc, A., & Clough, G. (1968). Behaviour of granular materials under high stresses. *Journal of the Soil Mechanics and Foundations Division*, *94*, 661–687.

Walton, K. (1987). The effective elastic moduli of a random packing of spheres. *Journal of the Mechanics and Physics of Solids*, *35*(2), 213–226. https://doi.org/10.1016/0022-5096(87)90036-6

Wang, H. (2000). *Theory of linear poroelasticity with applications to geomechanics and hydrogeology* (pp. 287). Princeton, NJ, USA: Princeton University Press.

Wang, B., Chen, Y., & Wong, T.-F. (2008). A discrete element model for the development of compaction localization in granular rock. *Journal of Geophysical Research*, *113*, B03202. https://doi.org/10.1029/2006JB004501

Wong, T.-F., & Baud, P. (2012). The brittle-ductile transition in porous rock: A review. *Journal of Structural Geology*, *44*, 25–53. https://doi.org/10.1016/j.jsg.2012.07.010

Wong, T.-F., David, C., & Zhu, W. (1997). The transition from brittle faulting to cataclastic flow in porous sandstones: Mechanical deformation. *Journal of Geophysical Research*, *102*(B2), 3009–3025. https://doi.org/10.1029/96JB03281

Wong, T.-F., Szeto, H., & Zhang, J. (1992). Effect of loading path and porosity on the failure mode of porous rocks. *Applied Mechanics Reviews*, *45*(8), 281–293. https://doi.org/10.1115/1.3119759

Wu, H., Guo, N., & Zhao, J. (2018). Multiscale modeling and analysis of compaction bands in high-porosity sandstones. *Acta Geotechnica*, *13*(3), 575–599. https://doi.org/10.1007/s11440-017-0560-2

Xiao, X., & Evans, B. (2003). Shear-enhanced compaction during non-linear viscous creep of porous calcite quartz aggregates. *Earth and Planetary Science Letters*, *216*(4), 725–740. https://doi.org/10.1016/S0012-821X(03)00536-3

Yin, H., & Dvorkin, J. (1994). Strength of cemented grains. *Geophysical Research Letters*, *21*(10), 903–906. https://doi.org/10.1029/93GL03535

Zhang, J., Wong, T.-F., & Davis, D. M. (1990). Micromechanics of pressure-induced grain crushing in porous rocks. *Journal of Geophysical Research*, *95*(B1), 341–352. https://doi.org/10.1029/JB095iB01p00341

Zoback, M. D., & Byerlee, J. D. (1975). The effect of cyclic differential stress on dilatancy in westerly granite under uniaxial and triaxial conditions. *Journal of Geophysical Research*, *80*(11), 1526–1530. https://doi.org/10.1029/JB080i011p01526

Zoback, M. D., & Byerlee, J. D. (1976). Effect of high-pressure deformation on permeability of Ottawa Sand. *AAPG Bulletin*, *60*(9), 1531–1542.